

Article

Strain Rate Dependence and Recrystallization Modeling for TC18 Alloy during Post-Deformation Annealing

Zhaosen Li ¹, Jinyang Ge ¹, Bin Kong ², Deng Luo ³, Zhen Wang ³ and Xiaoyong Zhang ^{1,*}

¹ State Key Laboratory of Powder Metallurgy, Central South University, Lu Mountain South Road, Changsha 410083, China

² Hunan Xiangtuo Goldsky Titanium Metal Co. Ltd., No. 116, Linyu Road, Yuelu Zone, Changsha 410221, China

³ Xiangtan Iron & Steel Group Co. Ltd., Yue Tang District, Xiangtan 411104, China

* Correspondence: zhangxiaoyong@csu.edu.cn

Abstract: In this paper, the dependence of dynamic recrystallization (DRX) and post-dynamic recrystallization (PDRX) of TC18 alloy on strain rate within the range of $0.001\text{ s}^{-1}\sim 1\text{ s}^{-1}$ was investigated through isothermal compression and subsequent annealing in the single-phase region. Electron backscatter diffraction (EBSD) characterization was employed to quantify microstructure evolution and to reveal the recrystallization mechanism. At the thermo-deformation stage, the DRX fraction does not exceed 10% at different strain rates, due to the high stacking fault energy of the β phase. During the subsequent annealing process, the total recrystallization fraction increases from 10.5% to 79.6% with the strain rate increasing from 0.001 s^{-1} to 1 s^{-1} . The variations in the geometrically necessary dislocation (GND) density before and after annealing exhibit a significant discrepancy with the increasing strain rate, indicating that the GND density is a key factor affecting the PDRX rate. The PDRX mechanisms, namely meta-dynamic recrystallization (MDRX), continuous static recrystallization (CSRX) and discontinuous static recrystallization (DSRX), were also revealed during the annealing process. A new kinetic model coupling DRX and PDRX was proposed to further describe the correlation between recrystallization and the strain rate during continuous deformation and annealing. This new model facilitates the prediction of recrystallization fraction during isothermal deformation and annealing of titanium alloys.



Citation: Li, Z.; Ge, J.; Kong, B.; Luo, D.; Wang, Z.; Zhang, X. Strain Rate Dependence and Recrystallization Modeling for TC18 Alloy during Post-Deformation Annealing. *Materials* **2023**, *16*, 1140. <https://doi.org/10.3390/ma16031140>

Academic Editor: Daniela Kovacheva

Received: 5 January 2023

Revised: 24 January 2023

Accepted: 27 January 2023

Published: 29 January 2023



Copyright: © 2023 by the authors. Licensee MDPI, Basel, Switzerland. This article is an open access article distributed under the terms and conditions of the Creative Commons Attribution (CC BY) license (<https://creativecommons.org/licenses/by/4.0/>).

Keywords: TC18 alloy; strain rate; post-deformation annealing; post-dynamic recrystallization; kinetic model

1. Introduction

Near β titanium alloys are attractive materials for aerospace applications due to their high strength and good workability [1–4]. Subtransus and supertransus thermomechanical processing (TMP) are widely used for titanium alloys in order to obtain the desired microstructure and properties that meet the service conditions. The TMP process above the transus temperature can achieve a β grain refinement by breaking the as-cast microstructure. Numerous studies have shown that dynamic recovery (DRV) and dynamic recrystallization (DRX) are the main mechanisms during supertransus thermal deformation [5–8]. However, for large billets, the core temperature drops very slowly at the end of deformation, which is equivalent to experience a period of annealing. Further recrystallization occurs, for instance, meta-dynamic recrystallization (MDRX) originated from DRX grains and static recrystallization (SRX) merged by recrystallization nucleation and sub-grains rotation [9,10]. They are also collectively referred to as post-dynamic recrystallization (PDRX), that have a great influence on microstructural uniformity [11,12].

The PDRX behavior during the annealing process is influenced by the historical deformation and annealing parameters. It has been widely reported in some materials, such as

aluminum alloy, Inconel, steels, etc. Zhang et al. [13] studied the PDRX behavior of 7055 aluminum alloy using a two-pass isothermal compression test, and found that the long pass interval time was beneficial for finer grain during the pass interval period. Chen et al. [14] investigated the recrystallization of 30Cr2Ni4MoV steel during hot deformation and revealed that a high temperature and larger strain rate had a strong effect on the PDRX of the material. A. Després et al. [15] found that the PDRX grains were growing rapidly because of a high strain rate during the annealing process, which could be as short as a few seconds to achieve full recrystallization in Inconel 718. Nicolaÿ et al. [16] reported that at high strain rates, the microstructure evolution after deformation was mainly dependent on MDRX. At the low strain rate of 0.001 s^{-1} , SRX was shown to be the dominant mechanism.

In addition, some kinetic models were further established to describe the correlation between recrystallization and deformation conditions. Shi et al. [17] calculated the kinetic equations of PDRX by two-stage hot compression, and found that the increase of the strain rate and deformation could promote the occurrence of PDRX in LZ50 steel, which had a high fit with the simulation results of the CA method. Tang et al. [18] developed a model to characterize the microstructure evolution of TiAl alloy during PDRX using double-hit and triple-hit hot compression tests at $1150 \text{ }^\circ\text{C}$ under the strain rate of 0.001 s^{-1} , and found that the thermal deformation conditions had different effects on each evolutionary mechanism during the post-deformation annealing process. Ding et al. [19,20] found that the fraction of PDRX identified by the two-stage hot compression tests was not applicable in high-level stacking fault energy materials. It could also affect the accuracy of the kinetic model in materials, such as titanium alloy. Hence, a new method is proposed based on electron backscatter diffraction with the grain orientation spread approach as a direct measurement technique to calculate the PDRX fraction and establish a kinetic model.

Up until now, the conventional understanding of PDRX behavior has mostly focused on materials with a low to medium stacking fault energy (SFE), because DRX is the main mechanism in their thermal deformation [19]. However, titanium alloys, as a medium to high SFE material, are dominated by DRV during thermal deformation, but the presence of DRX also plays a non-negligible role in microstructure evolution [7,20]. Meanwhile, due to the narrow processing window and high strain rate sensitivity of titanium alloys, the fraction of DRX was found to be strongly influenced by the strain rate in some studies [4,7,21]. Therefore, detailed studies of the PDRX behavior of titanium alloys at different strain rates are quite necessary.

In this paper, the effect of the strain rate on the PDRX behavior of TC18 alloy was systematically investigated by thermal simulation compression experiments and the potential mechanism of annealing condition on PDRX was revealed. Furthermore, the kinetic model of recrystallization for TC18 alloy was established based on the DRX and PDRX theory. The changes in grain boundaries, grain size, grain orientation spread (GOS), geometrically necessary dislocations (GNDs) density, etc., during PDRX were characterized and investigated.

2. Experiments Materials and Procedure

2.1. Materials

The material studied in this paper is TC18 alloy, the actual chemical compositions (wt.%) are as follows: 5.20Al, 4.92Mo, 4.96V, 1.05Cr, 0.96Fe and balance Ti. The phase transition temperature of the alloy is approximately $875 \pm 5 \text{ }^\circ\text{C}$. Prior to the isothermal compression, the alloy cut from the forged bars was treated in a solid solution at $900 \text{ }^\circ\text{C}$ for 30 min to obtain the single β phase microstructure, followed by water quenching. The initial microstructure of the sample is shown by the inverse pole figure (IPF) map in Figure 1a, which consists of equiaxed β grains. It illustrates the distributions of low-angle grain boundaries (LAGBs, $2\text{--}15^\circ$, white lines) and high-angle grain boundaries (HAGBs, $>15^\circ$, black lines) in the primitive microstructure. Figure 1b shows the β grain size distribution, and the average initial grain size is about $253 \text{ }\mu\text{m}$.

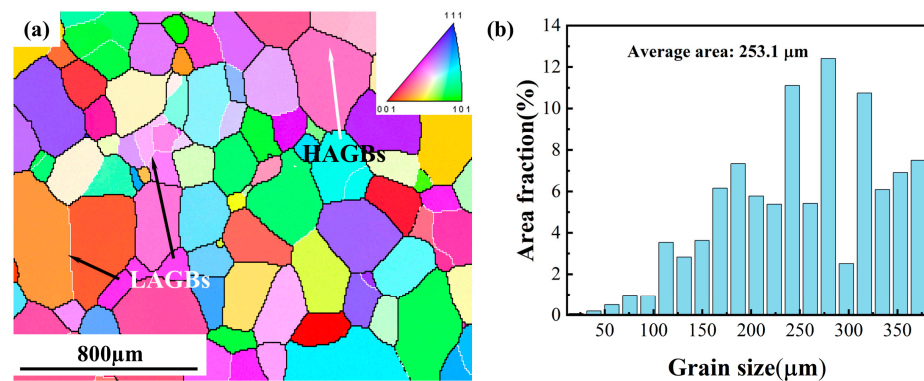


Figure 1. Initial microstructure of the TC18 alloy: (a) IPF map; (b) grain size distribution.

2.2. Experimental Methods

The cylindrical specimens of 10×15 mm used for the compression tests were cut from the solution-treated billet and then mechanically polished. The isothermal compression experiment was performed on a Gleeble 3180 thermos-mechanical simulator. Figure 2 shows the detailed procedure of the hot compression test. Following the heating at 5°C/s , the specimens were held at the deformation temperature for 5 min to ensure a uniform temperature distribution within the specimen before deformation. The deformation temperature was 900°C and strain rates ranged from 0.001 to 1 s^{-1} . Then, the specimens were compressed to the same deformation degree (50%), followed by annealing for 0–600 s and quenching. To eliminate as much friction as possible generated during compression, the graphite plate was placed between the cylindrical sample and the clamping mold.

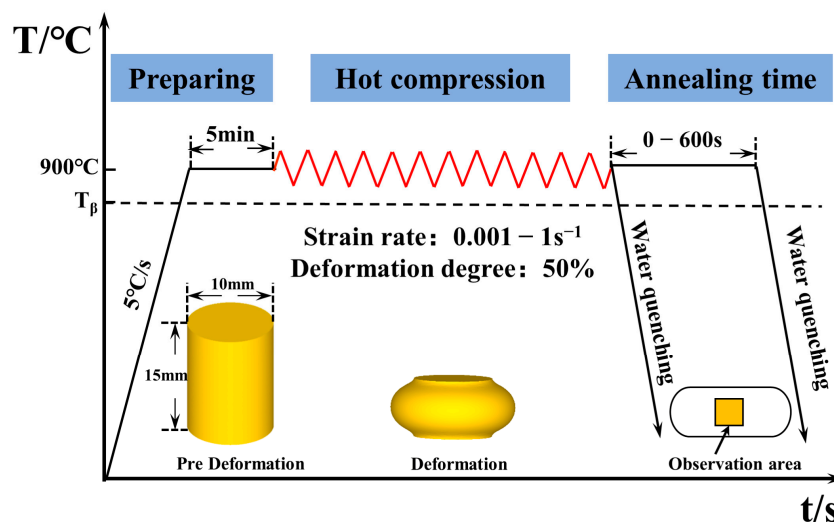


Figure 2. Experimental procedure of the thermal compression experiment.

2.3. Microstructure Characterization

Following the compression test, the samples were cut in half along the compression direction and subjected to microstructure characterization. Considering the non-uniform strain distribution in the deformed specimens, the central region of the specimen with the higher strain was chosen as the observation region. To ensure that the surface quality of the specimens meet the requirements of the EBSD analysis, the cut sections were first pre-polished with silicon carbide sandpaper and then electrolytic polished with the mixed solutions of 300 mL CH_3OH , 175 mL $\text{CH}_3(\text{CH}_2)_3\text{OH}$, 25 mL HClO_4 acid at a voltage of 60 V in a low-temperature environment. EBSD characterizations were carried out on a Helios Nanolab G3 UC scanning electron microscope. The scanned step length is $0.2\ \mu\text{m}$ at 15 kV of accelerating voltage and an accelerating current of 13 nA for EBSD. TSL-OIM

software was used to analyze the EBSD data of this work and to perform quantitative statistics. Recrystallized grains were distinguished by the grain orientation spread (GOS) method [20–22]. The geometrically necessary dislocation density (GND) was analyzed and quantitatively counted by MTEX-5.8.1 software [23,24].

3. Results

3.1. Dynamic Recrystallization Behavior during Thermal Deformation

IPF, GOS, and GND maps of the microstructure for TC18 alloy under different strain rates are shown in Figure 3. GOS is calculated by means of the average deviation between the orientation of each point within the grain and the grains' average orientation. As a result, the recrystallized grains can be distinguished from the deformed matrix according to the GOS index, and the percentage of recrystallization can be determined. Compared to the deformed grains, the recrystallized grains have lower GOS values, which are empirically considered to be <2 [25,26]. At the same time, the distribution of the dislocation density during this process can be visualized by GND diagrams, which are a reliable indication of the level of stored energy. Nye et al. [27] proposed the existence of GND to explain the plastic deformation mode. In combination with the corresponding GOS and GND maps, the specific microstructure evolution under different conditions can be determined. At the low strain rate of 0.001 s^{-1} (Figure 3a–c), larger DRX and irregular elongated grains with abundant sub-grains are identified in the microstructure. Grain boundaries bow out towards areas of high dislocation density and there is a large number of sub-grains within β -deformed grains, which demonstrates that the recovered and recrystallized grains have sufficient time to occur under this condition. With the strain rate increasing to 0.01 s^{-1} (Figure 3d–f), the fraction and size of equiaxial DRX grains are reduced. Meanwhile, the grain boundaries are serrated and DRV is reduced in this condition, characterized by the aggregation of most dislocations at deformed grain boundaries and the reduction of sub-grain boundaries. Small DRX grains occur at some trigonal grain boundaries. Further increasing the strain rate to 0.1 s^{-1} (Figure 3g–i), deformed grains are wider and seriously-elongated, and grain boundaries tend to be flattened. Few small equiaxial grains (showing low GND) locate at the serrated grain boundaries of the uniformly deformed specimen. At high strain rates of 1 s^{-1} (Figure 3j–l), the degree of grain boundary flattening is enhanced and exhibits a relatively high dislocation density. Some of the grain boundaries become serrated with the generation of sub-grains in β grains, and a few tiny equiaxial grains appear at the grain boundaries. The GND is relatively high in the elongated grains but is low in the tiny equiaxial grains (Figure 3l), suggesting the occurrence of DRX consumes the surrounding dislocation, and also indicating a severe degree of plastic deformation or high dislocation density in this region [28]. In addition, DRX grains are generated and grow up in places with large grain boundary undulations and at triple grain junctions, which is also known as discontinuous dynamic recrystallization (DDRX).

Figure 4 quantifies the DRX fraction as well as the percentage of LAGBs at different strain rates. As the strain rate increases from 0.001 to 1 s^{-1} , the dynamic recrystallization fraction decreases from 3.7% to 0.6%. Due to the reduction of deformation time, DRX is too late to nucleate and grow. However, LAGBs, as high-energy grain boundaries, to some extent, also reflect the magnitude of deformation energy storage. With the strain rate increasing from 0.001 to 0.1 s^{-1} , the percentage of LAGBs exhibits an opposite trend, increasing from 76.7% to 84.3%.

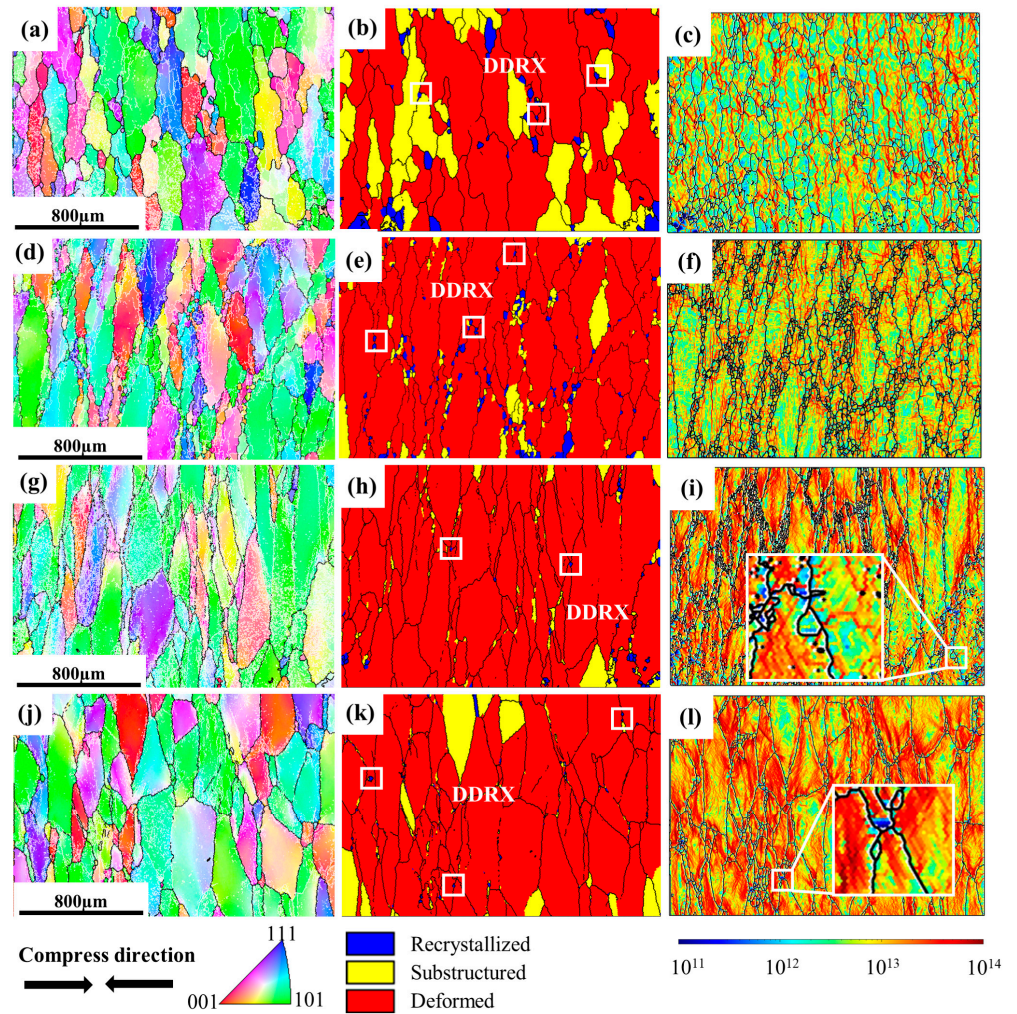


Figure 3. IPF, GOS and GND maps of the specimens deformed at different strain rates: (a–c) 0.001 s^{-1} ; (d–f) 0.01 s^{-1} ; (g–i) 0.1 s^{-1} ; (j–l) 1 s^{-1} .

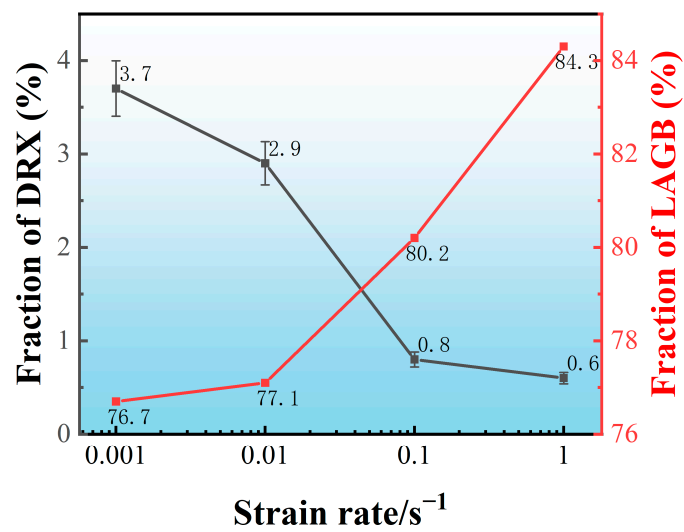


Figure 4. Quantitative analysis of the DRX and LAGB fraction of the specimens deformed at different strain rates.

3.2. Post-Dynamic Recrystallization Behavior during Post-Deformation Annealing

3.2.1. Effect of the Historical Strain Rate

Figure 5 shows IPF, GOS and GND maps of the microstructure for TC18 alloy after deformation at different strain rates and annealing for 600 s at 900 °C. Following the deformation at low strain rates of 0.001 s^{-1} and annealing (Figure 6a–c), the microstructure is still dominated by elongated β grains, and there are obvious misorientations and LAGBs in the internals of these grains, indicating that static recovery is the main mechanism for this condition. However, there are also a small number of recrystallized grains, approximately $80 \mu\text{m}$ of grain size at the serrated grain boundaries. Increasing the strain rate to 0.01 s^{-1} (Figure 6d–f), the elongated β grains are reduced and some recrystallized grains are observed to grow abnormally ($>200 \mu\text{m}$) in the annealing microstructure. A similar phenomenon was found in the study of Fan [29], which referred to the abnormal growth of grains during post-deformation annealing as MDRX, which is based on DRX grains for growth. When the strain rate increases to 0.1 s^{-1} (Figure 6g–i), the fraction of the recrystallization grains is sharply increased. However, elongated deformed grains still exist, and it is obvious that the GND values inside the deformed grains are relatively higher than that in the equiaxial recrystallized grains. However, some thick grains have slightly-elongated morphology and contain a small proportion of sub-grain boundaries formed by entangled dislocations (Figure 6i), demonstrating that SRV plays a key role when extensive SRX proceeds. As for the deformation at 1 s^{-1} (Figure 6j–l), further increases are observed in the fraction of recrystallization, along with an improvement in the homogeneity of the microstructure. Meanwhile, an interesting phenomenon is noted that recrystallized grains are found inside the deformed grains, which may be due to the gradual rotation of deformed sub-crystals during annealing, resulting in the migration of LAGBs to HAGBs.

Figure 6 quantifies the recrystallization fraction and the proportion of LAGBs, the relation of recrystallization fraction and the ratio of LAGBs exhibits similar patterns in other studies [7,11,30]. Annealing for the same time after deformation, as the strain rate increases from 0.001 to 0.01 s^{-1} , increases the recrystallization fraction from 10.5% to 20.2%. The recrystallization fraction increases greatly at high strain rates ($>0.01 \text{ s}^{-1}$), and it increases to 62.2% and 79.7%, respectively, when the strain rate increases to 0.1 and 1 s^{-1} . At the same time, the fraction of LAGBs decreases from 85.6% to 60.3%. LAGBs are converted to HAGBs gradually in this process. In addition, comparing the recrystallization fraction at the end of deformation, the recrystallization fraction during annealing increases as does the strain rate.

To further investigate the effect of the strain rate on the PDRX behavior of TC18 alloy, the variation of GND density after deformation and annealing was quantitatively analyzed. According to Nye's theory, which relates the rotational gradient within the Burgers circuit to the stored GND content, the GND density can be determined by the EBSD data [31,32]. It can be explained as [33]:

$$\rho_{GND} = 3KAM_{ave}/vb \quad (1)$$

where b is the Burgers vector, v is the step size taken for EBSD. KAM_{ave} denotes the mean misorientation in the core region. The GND density of TC18 alloy under different deformation conditions is calculated by the MATLAB program and the corresponding results are displayed in Table 1. The GND density is related to the strain rate during thermal deformation, with the maximum of 2.03 at 0.1 s^{-1} , and the minimum of 1.10 at 0.1 s^{-1} . This difference comes from the fact that the change in the strain rate affects the onset time of the dynamic recrystallization. The relationship between the GND density and strain rate in the annealing stage exhibits the opposite trend to that in the deformation stage, with the maximum of 1.05 at 0.001 s^{-1} , and the minimum of 0.29 at 0.1 s^{-1} . Dislocations, as a type of crystal defect, produce lattice disturbances in their vicinity in the form of strain. The increase in lattice strain leads to an increase in energy storage in the deformed material. Therefore, the dislocation density of the deformed matrix affects the driving force of post-recrystallization during subsequent annealing. High dislocation density facilitates recrystallization nucleation and growth, as shown in Figure 5. The consumption of GND

density during the annealing process corresponds to the change in recrystallization fraction at different strain rates, so that ΔGND is minimized at 0.001 s^{-1} .

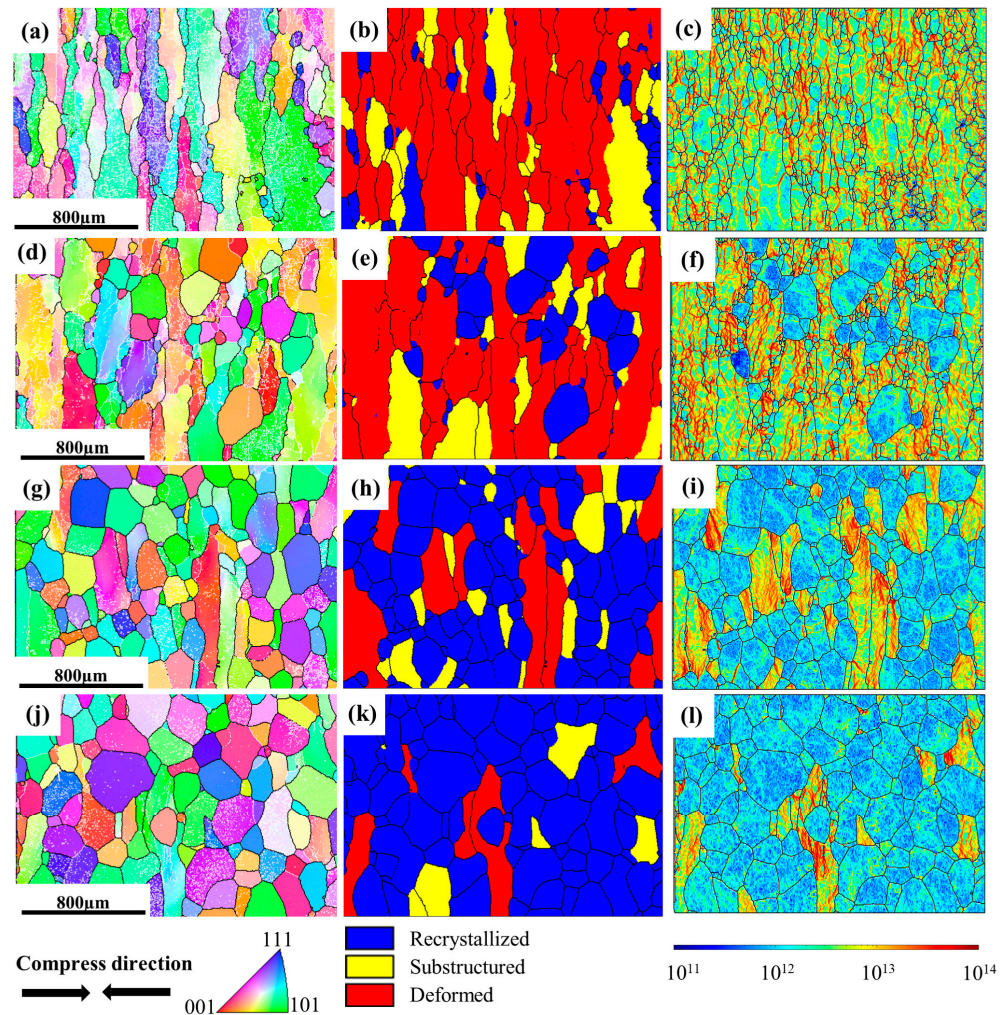


Figure 5. IPF, GOS and GND maps of the specimens deformed at different strain rates and then subjected to annealing for 600 s: (a–c) 0.001 s^{-1} ; (d–f) 0.01 s^{-1} ; (g–i) 0.1 s^{-1} ; (j–l) 1 s^{-1} .

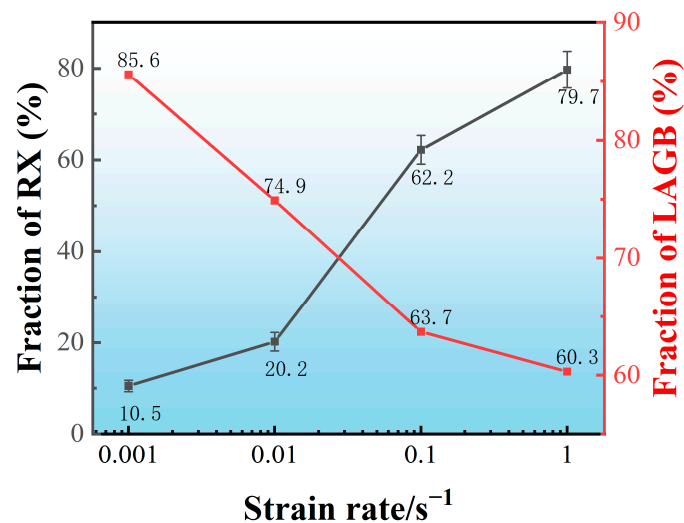


Figure 6. Quantitative analysis of the RX and LAGB fraction of the specimens deformed at different strain rates and then subjected to annealing for 600 s.

Table 1. Average GND density of the deformed titanium alloy under different conditions.

$\dot{\epsilon}/s^{-1}$	Deformation Degree/%	Average GND Density ($\times 10^{13}$)		
		Immediate Quenching	Annealing for 600 s	Δ GND
0.001	50	1.10	1.05	0.05
0.01	50	1.90	1.04	0.86
0.1	50	2.01	0.49	1.52
1	50	2.03	0.29	1.74

3.2.2. Effect of Annealing Time

To better understand the phenomenon of inhomogeneous recrystallization grain size under the deformation with the strain rate of $0.01 s^{-1}$ and subsequent annealing at $900\text{ }^{\circ}\text{C}$, microstructure evolution with annealing time was studied, as shown in Figure 7. The microstructure characteristics after deformation have been shown in Figure 3d,e. When the deformed specimen is held at $900\text{ }^{\circ}\text{C}$ for 60 s after deformation, the recrystallization fraction remains at about 3% and the grain size does not change significantly (Figure 7a,b). This indicates that post-dynamic recrystallization has not been initiated at this condition. Extending the annealing time to 300 s, recrystallized grains with different sizes appear around the deformed matrix, and the overall recrystallization fraction increases to 9.8%. This type of larger grain size can be distinguished by OIM analysis software for the PDRX orientation, which after practical analysis can be determined by an orientation difference of $0\text{--}0.5^{\circ}$, as shown in Figure 8a,b. The same phenomenon is also seen in the results of other studies, which refer to this recrystallization of larger grains during the annealing process as MDRX, i.e., DRX during deformation grain growth without a gestation period occurs during subsequent annealing and there is a significant gap in the grain size. This recrystallization grain growth mechanism is also referred to as the MDRX mechanism.

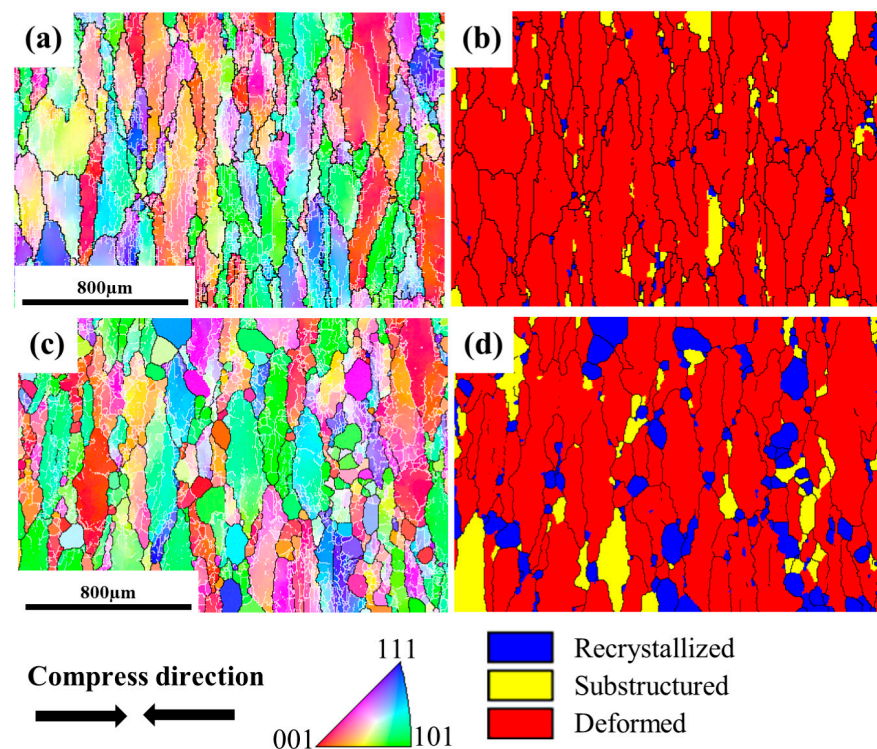


Figure 7. IPF and GOS maps of the specimens subjected to annealing for different times after deformation of 50% with the strain rate of $0.01 s^{-1}$: (a,b) 60 s; (c,d) 300 s.

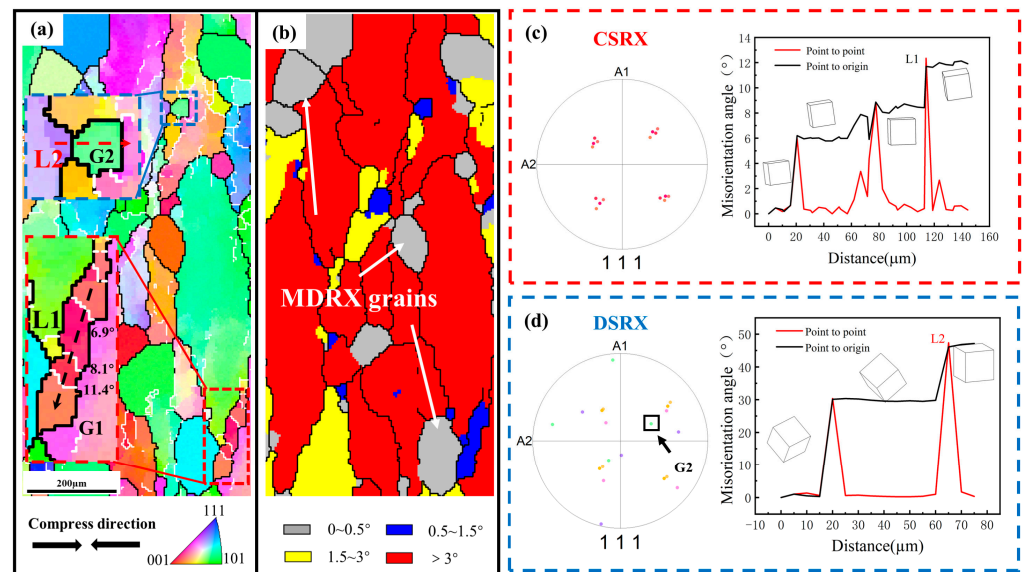


Figure 8. PDRX mechanism of TC18 alloy: (a) IPF map; (b) GOS map; (c) $\{111\}$ pole figure of G1 and misorientation change along L1; (d) $\{111\}$ pole figure of G2 and misorientation change along L2.

4. Discussion

4.1. Post-Dynamic Recrystallization Mechanism

The microstructure of the metal materials exhibits strong heritability during successive thermomechanical processing. Furthermore, the DDRX grains produced by thermal deformation are usually unstable at high temperatures, leading to the occurrence of MDRX during the subsequent annealing process, as the gray grains in Figure 8b. Ding et al. [20,34] distinguished between the DRX and MDRX grains through misorientation distribution. MDRX regards the previously generated DDRX grains as nuclei, which implies that MDRX no longer requires the nucleation step of conventional static recrystallization and grows rapidly in a short period of time. As a result, the grain size of MDRX grains is relatively larger than that of SRX grains during short-time annealing. For titanium alloys, the fraction of DRX during deformation in the single-phase region generally does not exceed 20%, due to the high stacking fault energy of the β phase. A high dislocation density still exists in the deformed matrix, especially when increasing the strain rate (Figure 3). In the red enlarged area in Figure 8a, it can be observed that G1 contain sub-crystals within them, with a large number of small angular grain boundaries collecting at the sub-crystal boundaries and gradually forming new recrystallized grains, which pointed out that the accumulation of dislocations can act as a driving force for the sub-grain rotation [35]. The polar figure of G1, shown in Figure 8c, clearly illustrates the orientation relationship between them. The crystallographic orientation and color of these sub-grains are highly similar and show a gradual change. The black line L1 illustrates the path where the deformed grains are split into SRX grains by lattice rotation during annealing after isothermal compression, which is a typical CSRX feature. Thus, these microstructural evolutions support the occurrence of CSRX through dislocation transitions, static reversion to SRX, as well as sub-grain transitions merging from LAGBs to HAGBs.

In addition, small SRX grains can be observed to exist at the trigonal mouths of the initial grains, such as G2 in the blue enlarged area in Figure 8a. The HAGB of the curvature at larger deformation is bent toward the adjacent grains by the grain boundary-induced migration mechanism, so that the grain boundaries are bowed out from the low density to the high density and become stable interfaces after reaching a certain size, forming new small SRX grains. This fully exhibits the DSRX characteristics [36]. In addition, the dislocation relationship can further illustrate the DSRX mechanism, as shown in Figure 8d, the dislocation relationship between the grains and G2 in the polar figure proves that the DSRX grains have a random orientation. The red line L2 also proves that the lattice of G2,

compared with surrounding grains, has changed completely. In conclusion, it was shown that CSRX and DSRX are the main static recrystallization mechanisms in TC18 titanium alloy, which has also been reported in other titanium alloys [37].

Figure 9 illustrates the schematic diagram of the recrystallization mechanism during deformation and subsequent annealing. On the one hand, dislocations pile up near the grain boundaries, causing large distortion energy at the grain boundaries and promoting recrystallization nucleation during the deformation in the single-phase region. As the grain boundaries migrate, the grain boundaries produce bulges and gradually form DDRX. On the other hand, with the increase of strain, high dislocation density regions are also formed inside the grain. A large number of sub-grains are generated and accompanied by rotation. At the end of deformation and at the beginning of annealing, DDRX grains from the deformation stage absorb the surrounding distortion energy and grow rapidly, forming MDRX. With the extension of annealing time, driven by strain energy and interfacial energy, small DSRX grains are formed, which are distinguished from DDRX. At the same time, sub-grains inside the deformed grains rotate further and LAGBs gradually migrate to the HAGBs, forming CSRX. Finally, with a further extension of time, the dislocations annihilate and the deformed grains all become recrystallized grains under the action of different recrystallization mechanisms.

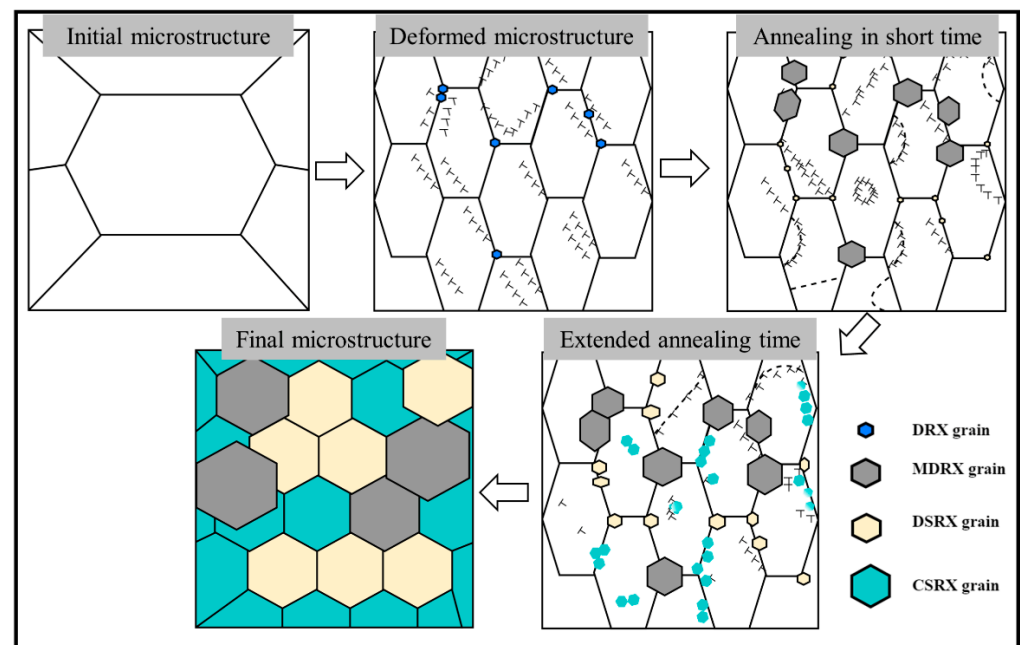


Figure 9. Schematic diagram of the post-dynamic recrystallization of TC18 alloy.

4.2. Recrystallization Kinetic Model

The strain rate affects not only the occurrence of DRX during deformation (Figure 3), but also the driving force of PDRX during annealing (Figure 5). In order to quantitatively describe the effect of the strain rate on recrystallization during successive deformation and annealing, a new recrystallization kinetic model is proposed. Recrystallization fractions of the specimens with different strain rates during the annealing process were supplemented, as shown in Table 2. The total recrystallization fraction is equal to the sum of DRX and PDRX [38];

$$X_{total} = X_{DRX} + X_{PDRX} \quad (2)$$

where X_{DRX} is the fraction of dynamic recrystallization at the end of deformation, X_{PDRX} is post-dynamic recrystallization during annealing.

Table 2. The fraction of DRX and total recrystallization under different strain rates.

$\dot{\varepsilon}/s^{-1}$	$X_{DRX}/\%$	X_{total} at Different Times/%			
		60 s	180 s	300 s	600 s
0.001	3.7	4.7	5.4	6.9	10.5
0.01	2.9	3.4	9.8	13.6	20.2
0.1	0.8	0.9	11.3	24.3	62.2
1	0.6	0.68	28.6	35.9	79.7

The DRX kinetic model generally established the connection between the DRX fraction and strain by strain–stress curves in most studies. Zhou et al. [39] improved the Avrami equation and coupled strain and strain rate describing the fraction, and the equation is as follows:

$$X_{DRX} = 1 - \exp \left[-\beta_d \left(\frac{\varepsilon - \varepsilon_c}{\dot{\varepsilon}} \right)^n \right] \quad (3)$$

where $\dot{\varepsilon}$ is the strain rate; ε is the deformation document; ε_c is the critical strain that can be obtained by the process hardening rate from the stress–strain curve (Figure 10a,b); β_d , n are material constants. Taking the natural logarithm for both sides of the equation, n can be evaluated from the slope of the linear fit of $\ln[-\ln(1 - X_{DRX})]$ and $(\frac{\varepsilon - \varepsilon_c}{\dot{\varepsilon}})$. Similarly, β_d can be calculated from the intercept in Figure 11a. Meanwhile, the critical strain varies with the strain rate. According to the model of Sellars [40], the critical strain at different strain rates can be expressed by the following equation:

$$\varepsilon_c = A \left[\dot{\varepsilon} \exp \left(\frac{Q}{RT} \right) \right]^k \quad (4)$$

where A and k are material constants; Q denotes the deformation energy during the deformation process, which can be determined as 188 kJ/mol in the research of Shi [7]; R is the gas constant (8.31 J/mol/K); T is the deformation temperature (K). To simplify the calculation by going to the natural logarithm on both sides of the formula, A and k can be obtained according to the linear fit of $\ln \varepsilon_c$ and $\ln \dot{\varepsilon}$ (Figure 11b). The DRX kinetic model is acquired.

During the annealing process, the main recrystallization mechanism is PDRX. As the annealing time extends, the recrystallization fraction is increased by consuming more deformation energy. Therefore, the fraction of PDRX at different strain rates can be calculated by Table 2 with the increase of annealing time, and the PDRX kinetics model can be constructed using the JMAK equation [41,42], as follows:

$$X_{PDRX} = 1 - \exp[-\beta_p t^m] \quad (5)$$

where t is the annealing time. m , β_p are material-related constants and obtained by calculating the average value under different strain rates in most studies. However, in this work, it was found that the growth rate of the PDRX fraction is closely related to strain rates. The kinetic index m and the coefficient β_p in Equation (5) are strongly related to the strain rate, as shown by the following equation:

$$m = A_1 \ln(\dot{\varepsilon}) + c_1 \quad (6)$$

$$\beta_p = A_2 \exp\left(\frac{-\ln(\dot{\varepsilon})}{A_3}\right) + c_2 \quad (7)$$

A_1 , A_2 , c_1 and c_2 are constant about the material. Therefore, a link between the PDRX fraction and strain rate can be established through m and β_p as a way to explain the PDRX behavior. Next, material constants, such as A_1 , A_2 , c_1 and c_2 can be obtained by combining the fit to Equations (5)–(7), as shown in Figure 11c,d.

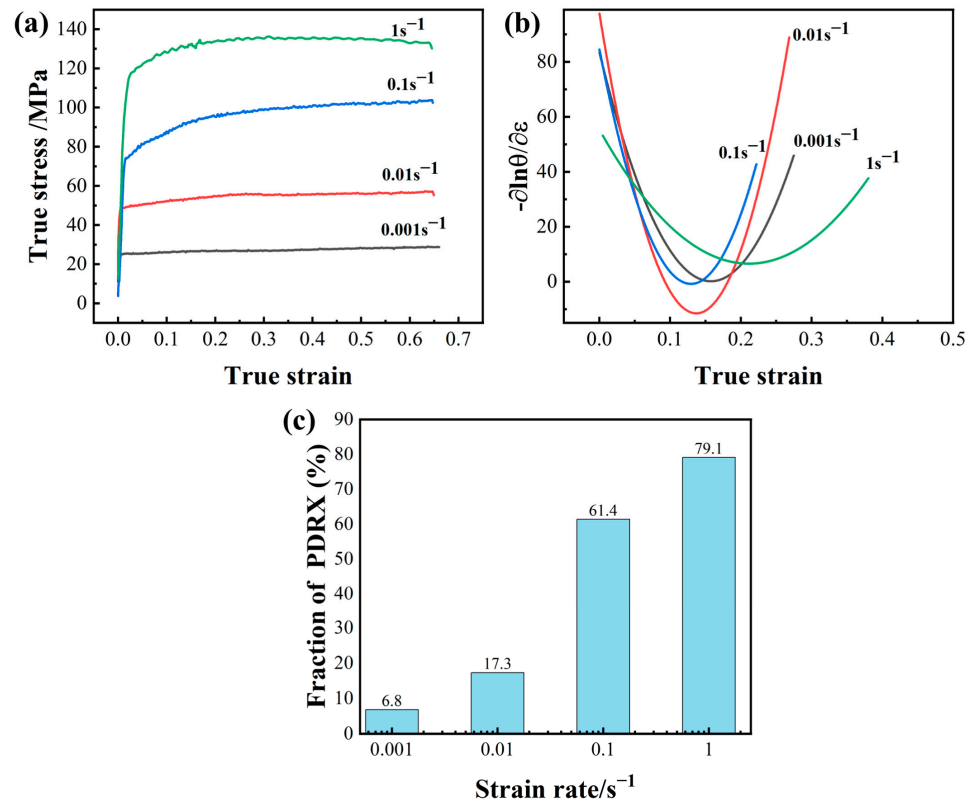


Figure 10. (a) Stress–strain curves at different strain rates; (b) Critical strain at different strain rates; (c) The fraction of PDRX at different strain rates.

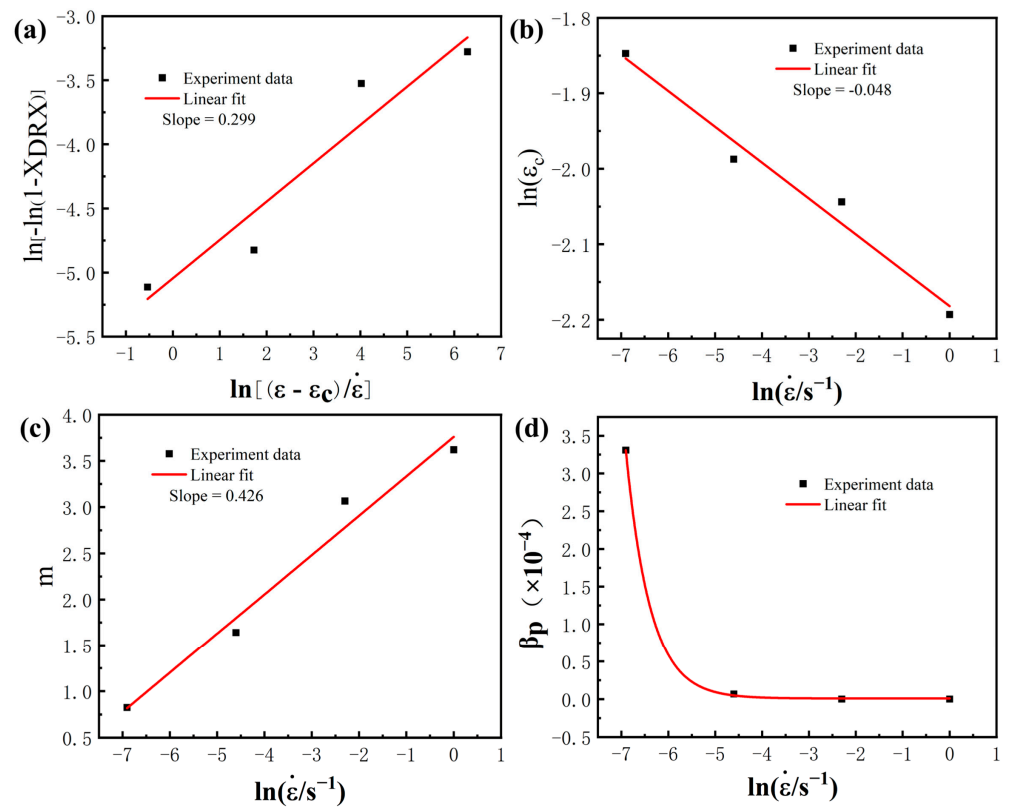


Figure 11. The fitting curves of (a) $\ln[-\ln(1-X_{DRX})]$ and $(\frac{\epsilon-\epsilon_c}{\dot{\epsilon}})$; (b) $\ln\epsilon_c$ and $\ln\dot{\epsilon}$; (c) n and $\ln\dot{\epsilon}$; (d) β_p and $\ln\dot{\epsilon}$.

In summary, the parameters solved in the above equation are shown in Table 3, and the recrystallization fraction equation for annealing at different times at different strain rates can be shown by the following equation:

$$X_{total} = 1 - \exp \left[-\beta_d \left(\frac{\varepsilon - A[\dot{\varepsilon} \exp(\frac{Q}{RT})]^k}{\dot{\varepsilon}} \right)^n \right] + 1 - \exp \left[-\left(A_2 \exp\left(\frac{-\ln(\dot{\varepsilon})}{A_3}\right) + c_2 \right) t^{A_1 \ln(\dot{\varepsilon}) + c_1} \right] \quad (8)$$

Table 3. The determined values of the material parameters.

n	β_d	A	k	A_1	C_1	A_2	A_3	C_2
0.299	6.45×10^{-3}	0.283	-0.048	3.76	0.426	5.8×10^{-10}	0.521	5.28×10^{-10}

To verify the accuracy of the recrystallization kinetic model, the recrystallization fractions were calculated for different times of annealing at different strain rates, and then the calculated values were compared with the predicted values in Figure 12. Standard statistical parameters, such as the correlation coefficient (R) can be expressed as follows:

$$R = \frac{\sum_{i=1}^N (E_i - \bar{E})(P_i - \bar{P})}{\sqrt{\sum_{i=1}^N (E_i - \bar{E})^2 \sum_{i=1}^N (P_i - \bar{P})^2}} \quad (9)$$

where E_i and P_i are the experimental and predicted recrystallization fraction, respectively. \bar{E} and \bar{P} are the mean values of E_i and P_i . N is the total number of data points used in the study. The linear correlation between experimental and predicted curves is defined by R , which ranges from -1 to 1 . The correlation would be better if the value is closer to 1 . Here, R is computed as 0.978 , indicating the high prediction accuracy of the developed constitutive model. Therefore, the recrystallization kinetic model is able to predict the recrystallization fraction at different strain rates very well.

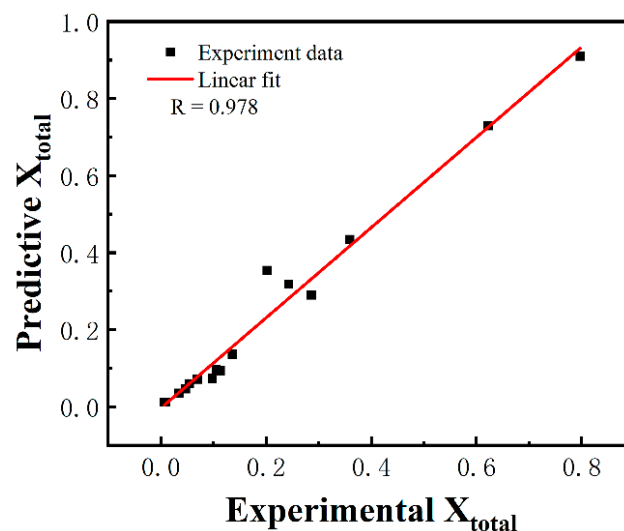


Figure 12. Comparison between the predicted and tested values of the recrystallization fraction.

5. Conclusions

The dependence of DRX and PDRX on the strain rate for TC18 alloy was investigated and the corresponding recrystallization model was also constructed during the post deformation annealing process. The main findings are summarized as follows:

- (1) During thermal deformation in the single-phase region, DRV is the dominant mechanism. As the strain rate increases from 0.001 s^{-1} to 1 s^{-1} , the DRX fraction decreases from 3.7% to 0.6%. The GND density in the deformed matrix is closely related to the strain rate, the higher the strain rate, the higher the GND density;
- (2) PDRX exhibits a distinct strain rate dependence. The variation of the PDRX proportion at different strain rates is accompanied by the variation of the GND density on the β matrix, indicating that PDRX occurs by absorbing the surrounding deformation storage energy;
- (3) Deformed and DRX grains undergo different mechanisms during the post-deformation annealing process. MDRX occurs rapidly through the preferential growth of DRX without the process of nucleation. The amount of MDRX is determined by the fraction of DRX during the deformation stage. Subsequently, DSRX by bulging of the grain boundaries and CSRX by sub-grain rotation emerges;
- (4) Based on the conventional JMAK kinetic equations, a new recrystallization model coupling DRX and PDRX during continuous deformation and annealing is proposed. The correlation coefficient (R) of the model is 0.978. Therefore, the model can accurately describe the correlation between the recrystallization and strain rate for TC18 alloy.

Author Contributions: Conceptualization, X.Z.; Methodology, B.K. and D.L.; Investigation, Z.L. and J.G.; Software, Z.L. and Z.W.; Formal analysis, Z.L. and J.G.; Funding acquisition, X.Z.; Project administration, X.Z., D.L. and Z.W.; Supervision, X.Z.; Writing—original draft, Z.L.; Writing—review & editing, J.G. and X.Z. All authors have read and agreed to the published version of the manuscript.

Funding: The authors would like to acknowledge the financial support from the National Natural Science Foundation of China (No. 51871242), the Innovative Province Construction Special Project of Hunan Province (2020GK4018), and the Technical Research Project of Hunan Province (2021GK1080).

Institutional Review Board Statement: Not applicable.

Informed Consent Statement: Not applicable.

Data Availability Statement: All raw data supporting the conclusion of this paper are provided by the authors.

Conflicts of Interest: The authors declare no conflict of interest.

References

1. Banerjee, D.; Williams, J.C. Perspectives on titanium science and technology. *Acta Mater.* **2013**, *61*, 844–879. [[CrossRef](#)]
2. Qu, F.S.; Zhou, Y.H.; Zhang, L.Y.; Wang, Z.H.; Zhou, J. Research on hot deformation behavior of Ti-5Al-5Mo-5V-1Cr-1Fe alloy. *Mater. Des.* **2015**, *69*, 153–162. [[CrossRef](#)]
3. Wang, Q.W.; Lin, Y.C.; Jiang, Y.Q.; Liu, X.G.; Zhang, X.Y.; Chen, D.D.; Chen, C.; Zhou, K.C. Precipitation behavior of a β -quenched Ti-5Al-5Mo-5V-1Cr-1Fe alloy during high-temperature compression. *Mater. Charact.* **2019**, *151*, 358–367. [[CrossRef](#)]
4. Chen, W.; Li, C.; Zhang, X.; Chen, C.; Lin, Y.; Zhou, K. Deformation-induced variations in microstructure evolution and mechanical properties of bi-modal Ti-55511 titanium alloy. *J. Alloy. Compd.* **2019**, *783*, 709–717. [[CrossRef](#)]
5. Premkumar, M.; Himabindu, V.; Banumathy, S.; Bhattacharjee, A.; Singh, A. Effect of mode of deformation by rolling on texture evolution and yield locus anisotropy in a multifunctional β titanium alloy. *Mater. Sci. Eng. A* **2012**, *552*, 15–23. [[CrossRef](#)]
6. Ghosh, A.; Sivaprasad, S.; Bhattacharjee, A.; Kar, S.K. Microstructure–fracture toughness correlation in an aircraft structural component alloy Ti-5Al-5V-5Mo-3Cr. *Mater. Sci. Eng. A* **2013**, *568*, 61–67. [[CrossRef](#)]
7. Shi, S.; Ge, J.; Lin, Y.; Zhang, X.; Zhou, K. High-temperature deformation behavior and recrystallization mechanism of a near beta titanium alloy Ti-55511 in β phase region. *Mater. Sci. Eng. A* **2022**, *847*, 143335. [[CrossRef](#)]
8. Tan, K.; Li, J.; Guan, Z.; Yang, J.; Shu, J. The identification of dynamic recrystallization and constitutive modeling during hot deformation of Ti55511 titanium alloy. *Mater. Des.* **2015**, *84*, 204–211. [[CrossRef](#)]
9. Sakai, T.; Belyakov, A.; Kaibyshev, R.; Miura, H.; Jonas, J.J. Dynamic and post-dynamic recrystallization under hot, cold and severe plastic deformation conditions. *Prog. Mater. Sci.* **2014**, *60*, 130–207. [[CrossRef](#)]
10. Zouari, M.; Logé, R.E.; Bozzolo, N. In Situ Characterization of inconel 718 post-dynamic recrystallization within a scanning electron microscope. *Metals* **2017**, *7*, 476. [[CrossRef](#)]
11. Qiao, S.; Wang, Y.; Lv, L.; Tan, G.; Cheng, T.; He, J. Post-dynamic recrystallization behavior of a powder metallurgy Ni-Co-Cr based superalloy under different deformation conditions. *J. Alloy. Compd.* **2022**, *898*, 162961. [[CrossRef](#)]

12. Koundinya, N.T.B.N.; Karnati, A.K.; Sahadevan, A.; Murty, S.N.; Kottada, R.S. Assessment of the post-dynamic recrystallization effects on the overall dynamic recrystallization kinetics in a Ni-base superalloy. *J. Alloy. Compd.* **2022**, *930*, 167412. [[CrossRef](#)]
13. Zhang, T.; Lu, S.H.; Zhang, J.B.; Li, Z.F.; Chen, P.; Gong, H.; Wu, Y.X. Modeling of the static recrystallization for 7055 aluminum alloy by cellular automaton. *Model. Simul. Mater. Sci. Eng.* **2017**, *25*, 065005. [[CrossRef](#)]
14. Chen, F.; Cui, Z.; Sui, D.; Fu, B. Recrystallization of 30Cr2Ni4MoV ultra-super-critical rotor steel during hot deformation. Part III: Metadynamic recrystallization. *Mater. Sci. Eng. A* **2012**, *540*, 46–54. [[CrossRef](#)]
15. Després, A.; Mithieux, J.D.; Sinclair, C.W. Modelling the relationship between deformed microstructures and static recrystallization textures: Application to ferritic stainless steels. *Acta Mater.* **2021**, *219*, 117226. [[CrossRef](#)]
16. Nicolai, A.; Fiorucci, G.; Franchet, J.; Cormier, J.; Bozzolo, N. Influence of strain rate on subsolvus dynamic and post-dynamic recrystallization kinetics of Inconel 718. *Acta Mater.* **2019**, *174*, 406–417. [[CrossRef](#)]
17. Shi, X.Z.; Du, S.W. Recrystallization Mechanism of LZ50 Steel and Cellular Automata Simulation. *J. Mech. Eng.* **2019**, *55*, 43–52.
18. Tang, X.; Wang, B.; Ji, H.; Fu, X.; Xiao, W. Behavior and modeling of microstructure evolution during metadynamic recrystallization of a Ni-based superalloy. *Mater. Sci. Eng. A* **2016**, *675*, 192–203. [[CrossRef](#)]
19. Ding, S.; Taylor, T.; Alam Khan, S.; Sato, Y.; Yanagimoto, J. Further understanding of metadynamic recrystallization through thermomechanical tests and EBSD characterization. *J. Mater. Process. Technol.* **2022**, *299*, 117359. [[CrossRef](#)]
20. Ding, S.; Khan, S.A.; Yanagimoto, J. Metadynamic recrystallization behavior of 5083 aluminum alloy under double-pass compression and stress relaxation tests. *Mater. Sci. Eng. A* **2021**, *822*, 141673. [[CrossRef](#)]
21. Gu, B.; Chekhonin, P.; Xin, S.; Liu, G.; Ma, C.; Zhou, L.; Skrotzki, W. Effect of temperature and strain rate on the deformation behavior of Ti5321 during hot-compression. *J. Alloy. Compd.* **2021**, *876*, 26–34. [[CrossRef](#)]
22. Wright, S.I.; Nowell, M.M.; Field, D.P. A review of strain analysis using electron backscatter diffraction. *Microsc. Microanal.* **2011**, *17*, 316–329. [[CrossRef](#)]
23. Bachmann, F.; Hielscher, R.; Schaeben, H. Texture Analysis with MTEX—Free and Open Source Software Toolbox. *Solid State Phenom.* **2010**, *160*, 63–68. [[CrossRef](#)]
24. Hawezy, D.; Biroasca, S. Disparity in recrystallization of α - & γ -fibers and its impact on Cube texture formation in non-oriented electrical steel. *Acta Mater.* **2021**, *216*, 117141.
25. Lu, T.; Dan, Z.H.; Li, T.J.; Dai, G.Q.; Sun, Y.Y.; Guo, Y.H.; Li, K.; Yi, D.Q.; Chang, H.; Zhou, L. Flow softening and microstructural evolution of near β titanium alloy Ti-35421 during hot compression deformation in the $\alpha+\beta$ region. *J. Mater. Res. Technol.* **2022**, *19*, 2257–2274. [[CrossRef](#)]
26. Liu, P.; Zhang, R.; Yuan, Y.; Cui, C.; Liang, F.; Liu, X.; Gu, Y.; Zhou, Y.; Sun, X. Microstructural evolution of a Ni-Co based superalloy during hot compression at γ sub-/super-solvus temperatures. *J. Mater. Sci. Technol.* **2021**, *77*, 66–81. [[CrossRef](#)]
27. Nye, J.F. Some geometrical relations in dislocated crystals. *Acta Metall.* **1953**, *1*, 153–162. [[CrossRef](#)]
28. Calcagnotto, M.; Ponge, D.; Demir, E.; Raabe, D. Orientation gradients and geometrically necessary dislocations in ultrafine grained dual-phase steels studied by 2D and 3D EBSD. *Mater. Sci. Eng. A* **2010**, *527*, 2738–2746. [[CrossRef](#)]
29. Fan, X.G.; Yang, H.; Gao, P.F.; Zuo, R.; Lei, P.H. The role of dynamic and post dynamic recrystallization on microstructure refinement in primary working of a coarse grained two-phase titanium alloy. *J. Mater. Process. Technol.* **2016**, *234*, 290–299. [[CrossRef](#)]
30. Dong, R.; Zhang, X.; Kou, H.; Yang, L.; Zhao, Y.; Hou, H. Texture evolution associated with the preferential recrystallization during annealing process in a hot-rolled near β titanium alloy. *J. Mater. Res. Technol.* **2021**, *12*, 63–73. [[CrossRef](#)]
31. Zisman, A.A.; Van Boxel, S.; Seefeldt, M.; Van Houtte, P. Gradient matrix method to image crystal curvature by processing of EBSD data and trial recognition of low-angle boundaries in IF steel. *Mater. Sci. Eng. A* **2008**, *474*, 165–172. [[CrossRef](#)]
32. Merriman, C.C.; Field, D.P.; Trivedi, P. Orientation dependence of dislocation structure evolution during cold rolling of aluminum. *Mater. Sci. Eng. A* **2008**, *494*, 28–35. [[CrossRef](#)]
33. Yan, Z.; Wang, D.; He, X.; Wang, W.; Zhang, H.; Dong, P.; Li, C.; Li, Y.; Zhou, J.; Liu, Z.; et al. Deformation behaviors and cyclic strength assessment of AZ31B magnesium alloy based on steady ratcheting effect. *Mater. Sci. Eng. A* **2018**, *723*, 212–220. [[CrossRef](#)]
34. Ding, S.; Zhang, J.; Alam Khan, S.; Sato, Y.; Yanagimoto, J. Metadynamic recrystallization in A5083 aluminum alloy with homogenized and as-extruded initial microstructures. *Mater. Sci. Eng. A* **2022**, *838*, 142789. [[CrossRef](#)]
35. Xu, J.; Zeng, W.; Sun, X.; Jia, Z. Microstructure evolution during isothermal forging and subsequent heat treatment of Ti-17 alloy with a lamellar colony structure. *J. Alloy. Compd.* **2015**, *637*, 449–455. [[CrossRef](#)]
36. Zhang, S.; Xi, M.; Liu, R.; Li, M.; Guo, X.; Gui, Y.; Wu, J. Fabricating Ti-22Al-25Nb intermetallic with ductility higher than 25% by advanced printing technique: Point-forging and laser-deposition. *Mater. Sci. Eng. A* **2022**, *850*, 143520. [[CrossRef](#)]
37. Wang, K.; Wu, M.; Yan, Z.; Li, D.; Xin, R.; Liu, Q. Microstructure evolution and static recrystallization during hot rolling and annealing of an equiaxed-structure TC21 titanium alloy. *J. Alloy. Compd.* **2018**, *752*, 14–22. [[CrossRef](#)]
38. Zhao, Q.; Lv, M.; Cui, Z. Investigation on transformation-related recrystallization behavior of Ti2AlNb-based alloy. *Intermetallics* **2021**, *138*, 107302. [[CrossRef](#)]
39. Zhou, P.; Ma, Q. Dynamic recrystallization behavior and constitutive modeling of as-cast 30Cr2Ni4MoV steel based on flow curves. *Met. Mater. Int.* **2017**, *23*, 359–368. [[CrossRef](#)]
40. Ouyang, D.L.; Lu, S.; Cui, X.; Wang, K.L.; Wu, C. Dynamic recrystallization of titanium alloy TA15 during β hot process at different strain rates. *Rare Met. Mater. Eng.* **2011**, *40*, 325–330.

41. Elwazri, A.M.; Essadiqi, E.; Yue, S. Kinetics of metadynamic recrystallization in microalloyed hypereutectoid steels. *ISIJ Int.* **2004**, *44*, 744–752. [[CrossRef](#)]
42. Dub, V.; Churyumov, A.; Rodin, A.; Belikov, S.; Barbolin, A. Prediction of grain size evolution for low alloyed steels. *Results Phys.* **2018**, *8*, 584–586. [[CrossRef](#)]

Disclaimer/Publisher’s Note: The statements, opinions and data contained in all publications are solely those of the individual author(s) and contributor(s) and not of MDPI and/or the editor(s). MDPI and/or the editor(s) disclaim responsibility for any injury to people or property resulting from any ideas, methods, instructions or products referred to in the content.